Combustion and Flame 255 (2023) 112899

Contents lists available at ScienceDirect

Combustion and Flame

journal homepage: www.elsevier.com/locate/combustflame

Soot nucleation in diffusion flames and the role of aromatic hydrocarbons

Kevin Gleason[1], Alessandro Gomez*

Department of Mechanical Engineering and Materials Science, Yale University, 9 Hillhouse Avenue, New Haven, CT 06520-8286, USA

ARTICLE INFO

Article history:
Received 5 February 2023
Revised 6 June 2023
Accepted 6 June 2023
Available online 11 July 2023

Keywords:
Soot
Counterflow
Diffusion flame
PAH
Fuel surrogate

ABSTRACT

We perform spatially resolved measurements of light scattering of soot in atmospheric pressure counterflow diffusion flames to complement previously reported data on soot pyrometry, temperature and gaseous species up to three-ring polycyclic aromatic hydrocarbons (PAHs). We compare two flames: a baseline ethylene flame and a toluene-seeded flame in which an aliquot of ethylene in the feed stream is replaced with 3500 ppm of pre-vaporized toluene. The goal is twofold: directly adding an aromatic fuel to bypass the formation of the first aromatic ring, widely regarded as the main bottleneck to soot formation from aliphatic fuels, and assessing the impact of a common component of surrogates of transportation fuels on soot formation. The composition of the fuel and oxidizer streams are adjusted to ensure invariance of the temperature-time history, thereby decoupling the chemical effects of the fuel substitution from other factors. The doping approach enables the comparison of very similar flames with respect to combustion products, radicals and critical precursors to aromatic formation (C2–C5 species), in addition to the temperature-time history. Doping with toluene boosts the aromatic content and soot volume fraction relative to the baseline ethylene flame, but, surprisingly, the soot number density and nucleation rate are affected modestly. As a result, the observed difference in volume fraction in the toluene-doped flame is reflective of larger initial particles at the onset of soot nucleation. The nucleation rate when soot first appears near the flame is of the same order as the dimerization rate of *single-ring* aromatics, in contrast with the expectation that the dimerization of larger PAHs initiates the process. Even though in and of itself nucleation contributes modestly to the overall soot loading, nucleation conditions the overall soot loading by affecting the size of the *initial* particle, which ultimately affects subsequent growth.

1. Introduction

There has been broad interest in assessing details of the soot formation process of aromatic hydrocarbons for multiple reasons: (1) they have a high tendency to soot, (2) they may offer a distinct path to soot bypassing the formation of the first aromatic ring that is the typical bottleneck of the aliphatic path to soot, and (3) they are reference fuels in the composition of surrogates of transportation fuels such as Diesel and jet fuel that are both rich in aromatic content [1–7].

In a recent article we characterized an ethylene baseline flame and a modified ethylene flame, that had been doped with 3500 ppm of toluene, in terms of temperature, species and soot volume fraction [7]. We quantified aromatic species to define critical pathways of PAH growth within our diagnostic constraints and the relative importance of different pathways such as Hydrogen Abstraction Carbon Addition (HACA) [8], PAH radical recombination, or radical chain reactions [9–12]. We also quantified small aliphatics contributing to cyclization and ring opening mechanism for aromatic parent fuels. Therefore, the comparison between the two fuels in these flames provides a convenient means to track quantitatively the *entire* evolution from parent fuel(s) to PAHs and eventually soot in a single flame environment. The doping approach, comparing and contrasting different fuels using a baseline flame and a doped variant, has the distinctive advantage of preserving a fixed temperature-time history, and fixing major combustion products and critical radicals (H, O, OH), bringing to the fore chemical kinetic effects brought about strictly by the dopant [4,13,14].

The present contribution introduces new measurements on soot using laser light scattering that, coupled with pyrometric measurements, enable a full characterization of soot in terms of volume fraction, dispersion exponent, particle size and number density,

* Corresponding author.
E-mail address: Alessandro.Gomez@yale.edu (A. Gomez).
[1] Current address: General Electric-Aerospace, 1 Neumann Way, Cincinnati, OH 45215, USA.

https://doi.org/10.1016/j.combustflame.2023.112899
0010-2180/

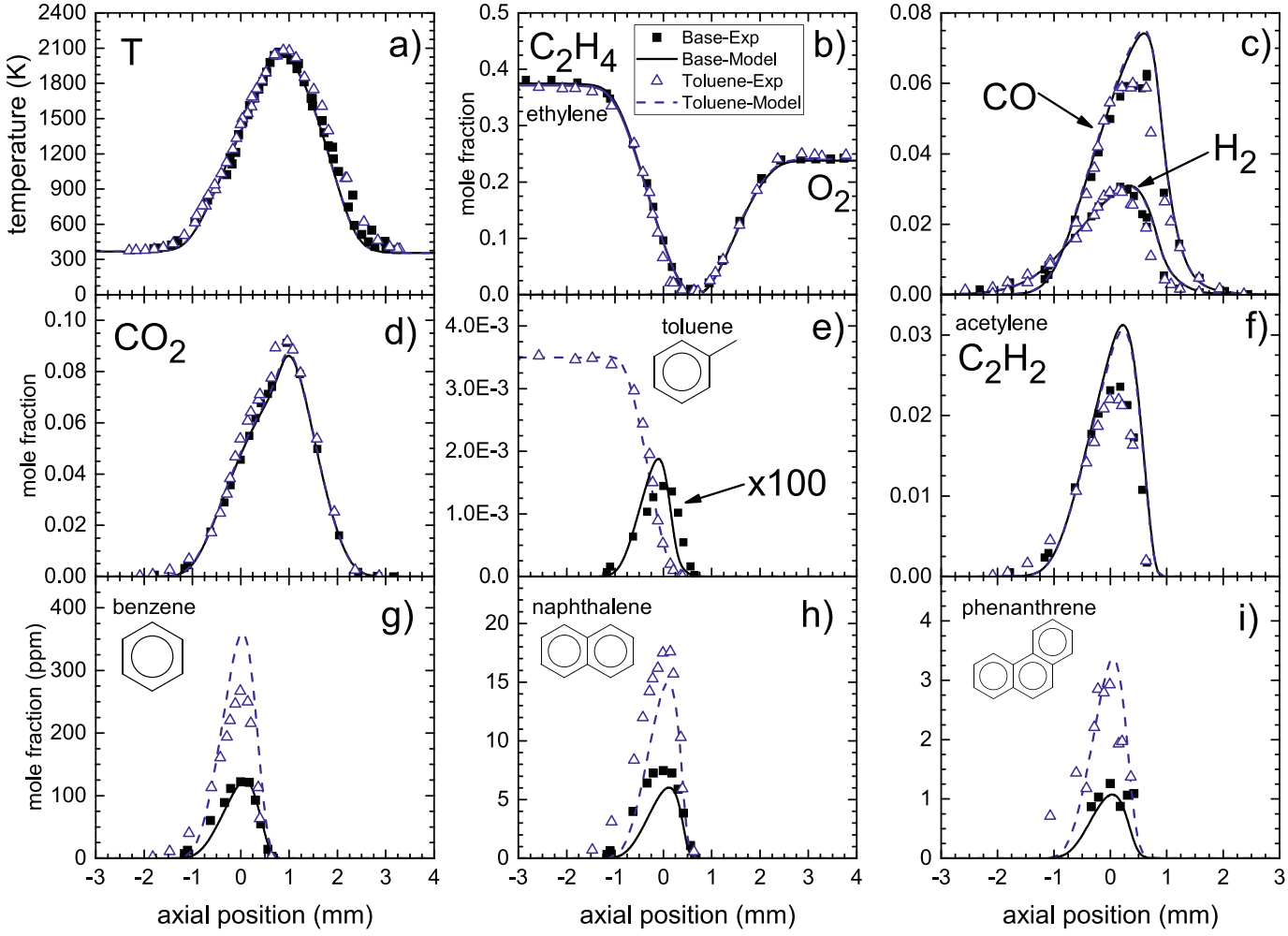

Fig. 1. Profiles of temperature (a) and mole fraction of reactants, major species and some key aromatics, including benzene, naphthalene, and phenanthrene (g–i), adapted from [7]. A factor of 100 is applied to the baseline flame in the toluene profile (e).

and, importantly, allow also for the assessment of the *soot nucleation rate* and its comparison with dimerization rates of aromatics, as in a previous study on an ethylene flame [15].

1.1. Major products, intermediates and aromatics

To orient the reader about the flame environment, this section briefly summarizes key measurements performed on the same flame, as reported in [7]. A probe connected to the injection port of a gas chromatograph/mass spectrometer system was used to extract gaseous samples and quantify H_2, O_2, N_2, CO, CO_2, and hydrocarbons up to three-ring PAH (190 amu). Temperature measurements were performed using a silica coated R-type thermocouple and applying standard corrections for radiative losses through a convective-radiative energy balance. Soot volume fraction and dispersion exponent measurements were performed by pyrometry using a digital camera with a calibrated spectral response. Details of the experimental approach are not repeated here since they are provided in [7,16]. The flames investigated are laminar and very stable, with flame flickering, as determined by the position of the flame chemiluminescence, confined to within the pixel resolution.

Profiles of temperature, reactants, major combustion products and key aromatics are adapted from Ref. [7] and reproduced in Fig. 1 to set the stage for further data analysis in the present article. For all figures, the baseline flame is shown with black solid symbols and lines and the toluene-seeded flame is shown with blue open symbols and dashed lines, the lines pertaining to model predictions. The abscissa in all plots is the distance from the gas stagnation plane (GSP), based on the computed velocity profile, with the fuel (oxidizer) stream on the left (right), represented by negative (positive) values of the axial position. Clearly, major combustion products and intermediates stem from the baseline ethylene flame and, with the exception of CO and C_2H_2 that are overpredicted by approximately 20% and 30%, respectively, [4,13] the effect of toluene-seeding is properly modeled. Since the baseline flame structure is not significantly affected, we can focus on the impact that doping has on the chemical pathways to soot and its precursors, with the expectation that the addition of an aromatic fuel with high sooting tendency should matter. The bottom row in Fig. 1 shows profiles of key aromatic compounds like benzene, naphthalene, and phenanthrene. Doping with toluene fuel increases the mole fraction of each species by a constant factor of two to three relative to the baseline ethylene flame. In both flames, the peak mole fraction decreases by approximately one order of magnitude with each additional ring suggesting that there is a sequential growth of PAHs [15,17]. Limitations in the detection limit of phenanthrene at 1 ppm prevent us from resolving the entire species profile in the baseline flame. Since experiments and model are in good agreement we can confidently explore production rates using a hybrid computational/experimental approach.

Table 1
Flame boundary conditions.

	Baseline	Doped
Fuel stream		
C_2H_4	0.375	0.371
N_2	0.625	0.625
C_7H_8	0ppm	3500 ppm
V_{avg}	27.2 cm/s	27.2 cm/s
V_{ax}	43.4 cm/s	43.4 cm/s
dV_r/dr	23.7 s^{-1}	23.7 s^{-1}
T	368 K	368 K
Oxidizer stream		
O_2	0.238	0.241
N_2	0.762	0.759
V_{avg}	28.8 cm/s	28.8 cm/s
V_{ax}	41.25 cm/s	41.25 cm/s
dV_r/dr	40.4 s^{-1}	40.4 s^{-1}
T	356 K	356 K
Flame properties		
T_{max}	2070 K	2079 K
Z_{st}	0.17	0.17
a (s^{-1})	70 s^{-1}	70 s^{-1}

2. Methods

2.1. Experimental diagnostics

2.1.1. Burner geometry and flame selection

The burner used consists of two identical converging nozzles oriented in counterflow configuration. The internal diameter of each nozzle is 6.35 mm and the nozzles are separated by 8 mm. Both nozzles are surrounded by a nitrogen shroud to shield the flame from external disturbances. We start with a baseline incipiently sooting diffusion flame of ethylene, feeding calibrated flows of ethylene/nitrogen and oxygen/nitrogen through the bottom and top nozzles, respectively. Momentum is unbalanced to position the flame front approximately centered between the burner nozzles, with $\rho_f V_f^2 = 1.2\rho_{ox}V_{ox}^2$ with obvious notation. The counterflow configuration provides a one-dimensional flow field in the vicinity of the burner axis, as confirmed by digital camera photographs showing a locally flat flame.

The maximum flame temperature, global strain rate, and stoichiometric mixture fraction are chosen to ensure that the soot scattering signal is distinguishable from that of the gas phase. This baseline flame is perturbed by replacing a small amount of ethylene with vaporized toluene, and adjusting the oxidizer composition to keep constant the stoichiometric mixture fraction $Z_{st} = 0.17$ and the global strain rate $a = 70s^{-1} = (V_{avg,f} + V_{avg,ox})/L$ in order to preserve the temperature-time history of the baseline flame. The bottom nozzle and fuel stream are heated to 368 K to prevaporize a spray of toluene injected with a syringe pump, and the preheat treatment is applied also to the baseline flame to ensure that the boundary conditions are otherwise identical. The amount of toluene added is such that the increase in soot load is distinguishable relative to the baseline flame. The difference in the computed peak flame temperature is less than 10 K, which is less than the experimental uncertainty. The boundary conditions of both flames are listed in Table 1, including molar composition, mass averaged velocity (V_{avg}) and axial velocity gradient (see Section 2.2), as well as measured temperature at the burner mouths.

2.1.2. Light scattering

Planar light scattering measurements are performed with the (532 nm) second harmonic of a 10 ns pulsed Nd:YAG laser (New Wave Gemini PIV). A cylindrical lens shapes the laser beam into a 4 mm by 1 mm sheet at the center of the burner with the laser fluence kept below 100 mJ/cm^2 to ensure that soot particles are not ablated by the high energy pulses [18]. The scattered light is imaged onto an intensified camera (12-bit PCO DiCAM-Pro) positioned at a 90° scattering angle, through an optical train including an 80 mm macro lens, a polarizer, and a 532 nm ± 10 nm interference filter. Data analysis is performed on an average of 500 images captured in a 20 ns gating window centered around the triggering of the laser pulse and background subtraction is applied by imaging the flame with the laser off. The gas-phase total light scattering coefficient of the investigated flames is calculated using the computed number concentration of H_2, H_2O, N_2, O_2, CH_4, CO, CO_2, C_2H_2, C_2H_4, C_2H_6, C_3H_8, C_3H_4, C_4H_6, and C_6H_6 whose scattering cross-section are reported in the literature [19–22]. All species accounted for in the gas phase scattering, except for H_2O, are measured and quantified with the GC/MS in both flames. The scattering cross section of toluene is assumed to be equal to that of benzene. The aforementioned species with a known scattering cross section are more than sufficient to characterize the total scattering coefficient of the gas phase [23]. Additionally, multiring PAHs whose scattering cross section is expected to be much larger than that of benzene appear at significantly lower concentrations, so their scattering contribution is expected to contribute little to the overall gas phase scattering coefficient.

Calibration gases (propane, ethylene, and nitrogen) are flowed through both top and bottom nozzles and imaged onto the intensified camera to verify that the appropriate ratios of the scattering coefficient are obtained. The calibration of any one gas ('*cal*') is used to convert the measured Rayleigh signal S to the scattering coefficient Q_{vv},

$$Q_{vv} = S_{meas}\frac{NC_{vv}^{cal}}{S_{cal}}, \tag{1}$$

where N is the local gas number density and C_{vv} is the scattering section of the calibration gas with the subscript 'vv' referring to both incident and scattered vertically polarized light. The soot number concentration N_s is evaluated under the hypothesis of size monodispersity as

$$N_s = \frac{9\pi^2 F(m) f_v^2}{Q_{vv}^{soot}\lambda^4}, \tag{2}$$

where Q_{vv}^{soot} is the measured excess scattering coefficient attributed to soot, net of the Rayleigh scattering contribution from the gas phase, f_v is the measured soot volume fraction via pyrometry [24], and $F(m) = 0.69 \pm 0.13$ is the dimensionless refractive index function at the laser wavelength $\lambda = 532$ nm based on the relationship between $F(m)$ and the dimensionless extinction coefficient [25]. The assumption of monodispersity in initial particle size is conservative in the sense that it minimizes the soot number density. The soot particle diameter is assumed spherical and evaluated by

$$d = \left(\frac{6f_v}{\pi N_s}\right)^{1/3}. \tag{3}$$

This assumption is reasonable in the high-temperature nucleation zone where particles nucleate but may become progressively weaker as particles evolve on their path towards the stagnation plane. Nevertheless, the small sizes measured by light scattering should preclude the existence of a large polydispersity in the soot particle population. Error bars based on 95% confidence are shown on every other symbol in Figs. 2 and 3, as computed from the measured signals of scattering coefficient and soot incandescence and applying general uncertainty analysis to propagate errors in the derived variables.

2.2. Flame modeling

One-dimensional modeling of the flames is performed with ANSYS CHEMKIN-Pro [26] using the KAUST chemistry Mechanism

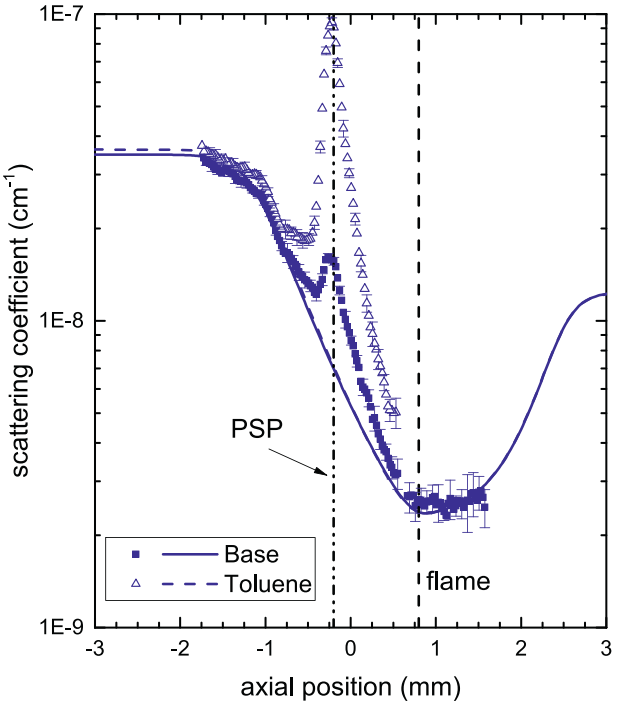

Fig. 2. Computed gas-phase scattering coefficient (lines) and measured scattering coefficient (symbols) for both investigated flames.

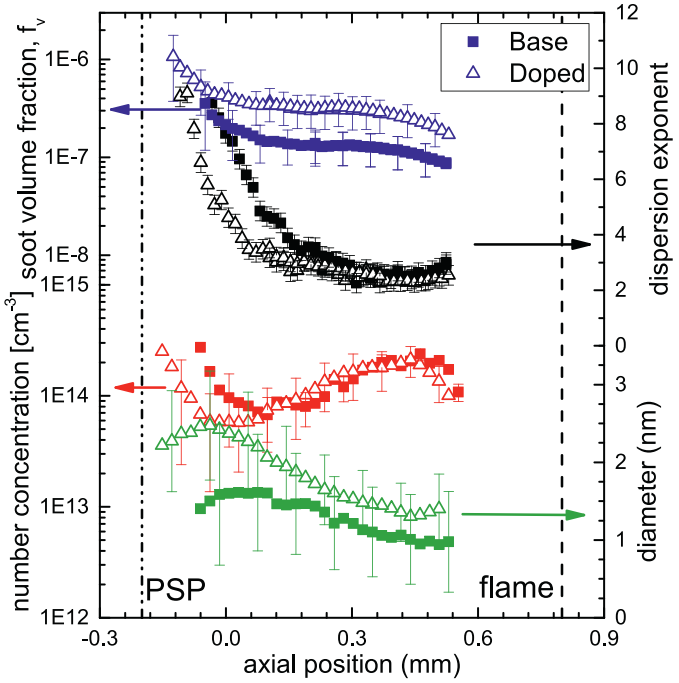

Fig. 3. Profiles of soot volume fraction and dispersion exponent (top), number concentration (middle) and particle size (bottom) for the baseline flame (full symbols) and the toluene-seeded flame (open symbols).

(KM2) [27]. We account for multicomponent diffusion coefficients, thermal diffusion, and thermal radiation of CO, CO_2, H_2O, and CH_4 in the optically thin limit. The KM2 mechanism was validated in a baseline flame up to 6-ring PAH [15] and partially validated for surrogate mixtures [28]. Two-dimensional modeling is performed in ANSYS to quantify the departure from plug flow. Briefly, we model the flow within the converging nozzle burner and shroud housing, including reactions using a simple 5-step mechanism, mixture-averaged transport, and buoyancy. The computed axial velocity (V_{ax}) and velocity gradient (dV/dz) from the 2-D simulations are provided in Table 1. The use of the simplified mechanism in the 2-D model is to account for the flames heat release which can influence the velocity profile at the burner exit. The 2-D simulation is identical to that described by Carbone et al. [29], except for the use of a different software.

3. Results and discussion

We begin with the measured scattering coefficient ($Q_{\nu\nu}$) shown in Fig. 2, which is taken as the average of approximately 250 µm (10 pixels) along the burner axis at each axial position. The soot forming region is located between the two vertical lines, the flame front shown as a dashed line on the right, and the particle stagnation plane shown as dash-dotted line on the left. The latter is the location where the sum of the axial velocity and the thermophoretic velocity is zero. The thermophoretic velocity is calculated by $V_{th} = -0.538\nu\nabla \ln(T)$ [30], using the model to determine temperature gradient and kinematic viscosity (ν). The blue lines represent the calculated gas-phase scattering contribution, $Q_{\nu\nu}^{gas}$, based on the computed molar fraction of the 14 species listed in the previous section. The toluene flame is represented by a blue dashed line, in which we assumed that the scattering cross section of toluene is equal to that of benzene. Within the soot forming region and on the oxidizer side of the flame, both the toluene flame and baseline flame gas-phase scattering coefficients are identical. On the fuel side, the gas-phase scattering coefficient of the toluene flame is less than 4% larger than that of the baseline flame and the overlapping experimental data are in good agreement with the calculated $Q_{\nu\nu}^{gas}$ in regions devoid of soot which gives us confidence that there is negligible error in the assumed scattering cross section of toluene.

The experimental data, shown in symbols in Fig. 2, are truncated when either the scattered signal is within 10% of the background noise or the finite dynamic range of the intensified camera makes it impossible to quantify $Q_{\nu\nu}^{gas}$ in the region devoid of soot. In the soot forming region, the measured scattering coefficient departs from the calculated gas-phase. The difference between the measured $Q_{\nu\nu}$ and $Q_{\nu\nu}^{gas}$ can be attributed confidently to soot, which reaches a maximum at the particle stagnation plane and drops sharply on the fuel side of the PSP where no soot is present. Comparing the scattering coefficient of the two flames, the toluene flame peaks at almost one order of magnitude higher than the baseline flame. Coupling these light scattering measurements with the measured volume fraction [7] will allow us to compare quantitatively the two flames in terms of soot number concentration and particle size.

3.1. Soot

Figure 3 presents profiles of measured soot volume fraction and dispersion exponent of both flames from pyrometry measurements. They were presented in the same article from which the data of Fig. 1 were adapted [7]. Vertical lines mark the position of the flame front and particle stagnation plane as in Fig. 2. The soot volume fraction profiles of both flames are qualitatively similar, but values for the toluene-seeded flame are approximately a factor of two larger than those of the baseline flame through most of the domain, which is not surprising in view of the marked increase in mole fraction of soot precursors (see Fig. 1 and ref. [7]). The region between GSP at the origin and PSP is an exception. In that region, approaching the GSP from the right, the dispersion exponent increases first for the baseline flame and closer to the GSP also for the doped flame. This is attributed to a low-temperature

soot forming mechanism resulting in the formation of new particles with large H/C content which is reflected by the larger dispersion exponent [16]. These freshly formed particles, dominated by PAHs or mixtures of PAHs and aliphatics, are more transparent in the visible spectrum [31,32] and small PAHs can be important for soot surface growth [33]. The concentration of PAHs peak in proximity of the GSP [7] (see also Fig. 5, discussed below), precisely where the increase in dispersion exponent occurs.

The introduction of scattering measurements enables us to quantify soot number density and particle size from Eqs. (2) and (3) with the assumption of particle monodispersity; corresponding profiles are shown in the bottom half of Fig. 3. Because of the composition of the feed streams, the flame is positioned on the oxidizer side of the gas stagnation plane. As soot particles nucleate near the flame front, in the absence of oxidizers they grow in size on the path towards the PSP where they are convected away radially. The number concentration profile appears to be initially shifted by less than 0.2 mm towards the PSP in the doped flame. The number concentration reaches a local maximum near the flame front, decreases because of coagulation as the residence time increase in the right-to-left direction toward the PSP, and rises again near the GSP where the above-mentioned low-temperature soot forming mechanism becomes dominant [16]. Clearly, the difference in volume fraction between the two flames is due largely to a difference in the *initial* particle sizes as shown at the bottom of Fig. 3. Importantly, such a difference is preserved through the entire domain as the particles first grow and eventually decrease in size near the GSP. We will revisit this point below in the discussion of Fig. 5.

3.2. Production rates

Since mole fraction and production rates of C_2H_2, the critical species in soot surface growth reactions via the HACA mechanism, are identical in the two flames, one may infer that the difference in volume fraction should be attributed to a difference in nucleation rate. However, the number concentration profiles in Fig. 3 do not seem to support this hypothesis.

To probe this aspect further, we compare nucleation *rates* in the two flames through the governing equation for the soot number concentration. As mentioned earlier, for the small particle sizes in question we can assume that the size distribution is monodisperse with reasonable accuracy in the nucleation region. Then, the nucleation rate in the axis-symmetric flow field can be expressed as,

$$\left.\frac{\partial N_S}{\partial t}\right|_{nucl} - \gamma_{coag}\sqrt{\frac{24k_BTd}{\rho_s}}N_s^2 = \frac{d}{dz}[N_s\cdot(V_z+V_{th}+V_P)] + N_s\cdot\frac{dV_r}{dr}. \tag{4}$$

On the LHS, the first term is the rate of change of the number of soot particles per unit volume, N_S, by nucleation and the second term is the destruction by coagulation of monodisperse particles in the free-molecular regime [34]. γ_{coag} is the collision efficiency, that is, the probability that particles stick together once they collide, and is assumed constant at 2% [15]. On the RHS of Eq. (4), the axial velocity V_z, radial velocity gradient dV_r/dr, and thermophoretic velocity V_{th} are determined from the model, with the particle Brownian velocity estimated by $V_P = -D_P\cdot\ d\ln(N_s)/dz$. The value of the Brownian diffusivity is calculated as a function of the measured particle diameter, d, by

$$D_P = \left(\frac{k_BT}{3\pi\,\rho_s\nu d}\right)\left[1+2Kn\left(A+B\ e^{-\frac{C}{Kn}}\right)\right], \tag{5}$$

with the Knudsen number, Kn, as the ratio of gas mean free path to particle diameter, A, B, and C empirical constants set equal to 1.257, 0.4, and 0.55, respectively [34]. The density of soot is assumed constant at ρ_s=1.5 g/cm^3, an intermediate value between the suggested density for nascent soot and mature soot (1.2 g/cm^3 and 1.8 g/cm^3, respectively) [32].

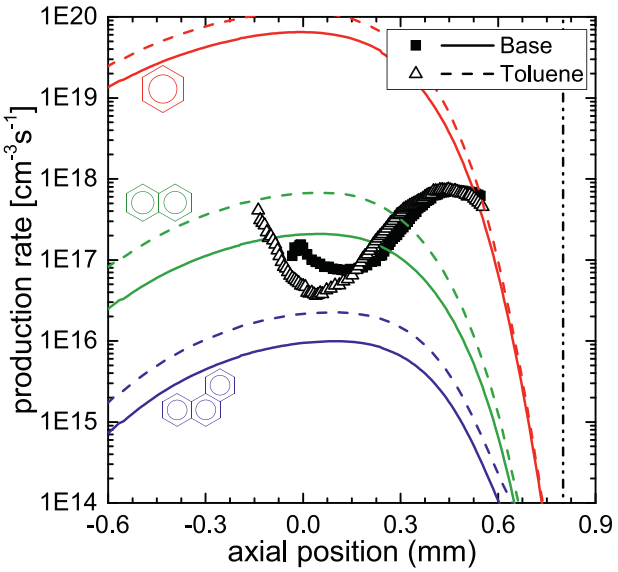

Fig. 4. Soot nucleation rate by assuming monodisperse particles and a coagulation efficiency of 2% with symbols as in Fig. 2. Lines are the calculated dimerization rate of benzene, naphthalene, and phenanthrene via kinetic theory of self-collision at a 1% collision efficiency. The baseline flame is shown in solid symbols and solid lines and the toluene-seeded flame is shown with open symbols and dashed lines.

The soot nucleation rate is compared to the irreversible dimerization rate that is based on the gas kinetic self-collision rate according to

$$\dot{\omega}_{DIM} = \eta\ 2.2\sqrt{\frac{4\pi\,k_BT}{M_{PAH}}}\sigma^2N_a^2[PAH]^2 \tag{6}$$

where η, k_B, N_a, M_{PAH}, σ, are the dimerization efficiency (i.e., the fraction of collisions that result in dimerization events), Boltzmann constant, the Avogadro number, the mass, and the collision diameter of the PAH under consideration, respectively [35]. The dimerization efficiency is assumed equal to 1% for all considered PAHs, which is likely an overestimate for these particularly small PAH structures, and the constant factor 2.2 is the van der Waals enhancement factor [8,36].

Production rates with dimensions of number density per unit time are shown in Fig. 4 based on Eqs. (4) and (6). The two flames are nearly identical also in terms of soot production rates, but the addition of toluene shifts the soot production rate slightly toward the fuel nozzle, as observed with the aromatic production rates (ref [7], Fig. 4 ibid). With a focus on the onset of soot, that is in the region closest to the flame front, we notice that the nucleation rate of soot is at the level of the benzene dimerization rate and orders of magnitude larger than that of both two- and three-ring (and even larger) PAHs. The results of Fig. 4 are consistent with the findings in [15,23] which investigated similar counterflow diffusion flames of ethylene at different pressures, with no doping but slightly different strain rate and Z_{st} at 50 s^{-1} and 0.18, respectively. The present data seem to suggest an even more restrictive interpretation with only the *single* ring aromatic accounting for the earliest stage of soot nucleation via aromatic dimerization and the dimerization rate of any larger aromatic, including putative precursors to soot, well below the production rate of soot. This result is consistent with the model in [33], concluding that dimers of benzene and other small PAHs contribute most to the total soot nucleation because of their relatively high concentration compared

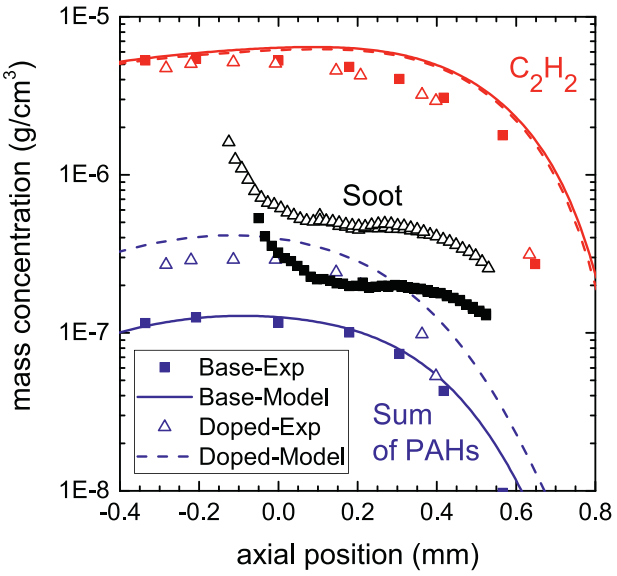

Fig. 5. Comparison of the mass concentration of C_2H_2, aromatics including benzene and PAHs, and soot.

to larger PAHs, even though the authors analyzed a different (premixed) flame. In fact, unmeasured larger species (pyrene, coronene, etc.) in the present study are expected to be at even lower concentrations if one considers that both flames appear to follow a sequential growth of PAHs [15,17] as opposed to the aromatic radical recombination route which would lead to larger PAHs appearing at higher concentration than smaller PAHs [12,37].

These findings apply to both the baseline flame of the aliphatic fuel and the toluene-seeded flame, which bears the question: what causes the increase in volume fraction in the toluene-seeded flame if even the nucleation rate of the two flames is not affected by the increase in PAH concentration and the subsequent dimerization rate?

To help answer this question, it is instructive to plot the mass concentration of soot, of all measured PAHs combined and benzene, as well as C_2H_2 in Fig. 5. The low concentration of aromatic species close to flame front makes it difficult to quantify them experimentally, but the model predicts at least a factor of two increase locally because of the toluene addition. This multiplier increases moving away from the flame front to a value slightly above three near the GSP where it peaks in both flames. The selection of the cumulative concentration of aromatics, including PAHs and benzene, stems from the consideration that we need to exclude toluene since it is the doping species whose concentration grows monotonically all the way to the fuel burner. However, path analysis in [7] shows that 33% of toluene evolves into mostly benzene and some phenyl radical and the remaining into benzyl radical or larger species (Fig. 7, ibid). As a result, the benzene concentration should account approximately also for the "active" toluene that is participating in the prevailing chemistry. Values for C_2H_2 are approximately one order of magnitude larger than those of soot and approximately two orders of magnitude larger than the mass concentration of aromatics in the high temperature nucleation zone close to the flame, for $z > 0.6$ mm. Benzene, partly derived from the doping with toluene, naphthalene, and phenanthrene account for more than 85% and 75% of the total mass in the baseline flame and the toluene-seeded flame, respectively, and another 28 species that were measured experimentally [7] account for the rest. Even considering only the three most abundant PAHs would not affect the data in Fig. 5 significantly. The reported total mass concentration of all PAHs should not be significantly biased because of the lack of quantification of larger PAHs since they would appear at sub-ppm concentrations.

Maintaining the focus on the zone where nucleation dominates over coagulation ($0.4\,\text{mm} < z < 0.8\,\text{mm}$), one is tempted to conclude that the low mass concentration of PAHs cannot account for the difference in the measured volume (and mass) fraction between the two flames. But, as observed in [15], the small concentration of PAHs may be merely indicative of a steady-state condition for this family of intermediates, which prevails if production rates and destruction rates are both large and comparable, so that the *net* production rate is very small [38]. So, even with a large production rate, PAHs are used up quickly through adsorption on the initial single-aromatic dimers via a comparably large "destruction" pathway ultimately leading to much larger peri–condensed PAHs that are needed to provide the necessary resonance stabilization and preclude their fragmentation. Details of how this stabilization occurs to overcome kinetic and thermodynamic constraints are not addressed in the absence of experimental data in the relevant size and mass range. It remains to be seen if accurate predictions of the consumption of the parent fuel components and the formation of small aromatic structures and acetylene suffice for soot modeling, with leeway on details of the intermediate growth to larger aromatic structures, which is much more challenging to model. All in all, the picture that emerges is consistent with the general view of soot inception and growth except for the fact that the very first step of the inception stage is the formation of dimers of *single* aromatic structures as opposed to larger PAHs. Recent modeling following prenucleation evolution of PAHs [39] support our experimental findings, at least for the case of two-ring aromatics [15].

Farther from the flame front, the sum of the aromatics concentration increases, approaching that of soot. This increase may explain the more rapid growth in soot mass in proximity of the PSP. A decrease in particle diameter and increase in soot number concentration in that region is indicative of the secondary low-temperature nucleation zone near the particle stagnation plane, as already mentioned in the context of Fig. 3, that can be rationalized based on dimerization of PAHs that exist in sufficient abundance to yield the measured soot. Although this last observation should be taken with the grain of salt since the assumption of size monodispersity may be questionable in that region, the sudden increase of the dispersion exponent confirms that nucleation of fresh particles plays a dominant role in that region.

The first detected particles (Fig. 3) are already the result of some growth of subnanometer embryos, since diagnostic limitations prevent the quantification of even younger soot particles. This initial growth is accelerated in the toluene-seeded flame leading to a larger particle at the first measurement location near the flame. After this phase, surface growth via the abundant C_2H_2 quickly overtakes and dominates soot. Since the mass concentration of C_2H_2 is essentially identical in the two flames, any difference in surface growth and ultimately particle size must be due largely to the difference in the *initial* nanoparticle size (and surface area). This observation is borne out of the data and facilitated by the comparison of very similar flames using the doping approach. As a result, even though nucleation per se contributes modestly to the soot loading in a flame, the importance of the initial phase of nucleation is apparent. Therefore, nucleation must remain a main focus of soot modeling for a correct quantification of soot loading in a flame.

4. Conclusions

An experimental study of a toluene-doped atmospheric pressure counterflow diffusion flame of ethylene shows unsurprisingly that replacing part of ethylene in a baseline flame with toluene

results in a marked overall increase in soot formation, consistently with the expectation that toluene pyrolysis leads readily to the formation of PAHs and bypasses the formation of the first aromatic ring as a potential bottleneck to soot formation. The comparison of the number nucleation rate of soot and dimerization rates of aromatic compounds suggests that nucleation is initiated by the (formation and/or) availability of *single-ring* aromatic compounds through a likely chemical clustering route, with larger PAHs playing a role only in the subsequent growth and stabilization of the dimer, in contrast with the longstanding hypothesis that chemical bond-building and clustering of relatively *large* aromatic systems triggers incipient soot. The comparison between very similar flames using the doping approach reveals the importance of the initial nucleation step that, even though intrinsically contributes modestly to the overall soot loading of the flame, determines not only the initial particle size but also conditions the soot loading.

Declaration of Competing Interest

The authors declare that they have no known competing financial interests or personal relationships that could have appeared to influence the work reported in this paper.

Acknowledgments

The authors acknowledge the support of the National Science Foundation (CBET-1853150) and declare no competing interests.

References

[1] M. Gu, F. Liu, J.L. Consalvi, Ö.L. Gülder, Effects of pressure on soot formation in laminar coflow methane/air diffusion flames doped with n-heptane and toluene between 2 and 8 atm, Proc. Combust. Inst. 38 (2021) 1403–1412.
[2] S. Jahangirian, C.S. McEnally, A. Gomez, Experimental study of ethylene counterflow diffusion flames perturbed by trace amounts of jet fuel and jet fuel surrogates under incipiently sooting conditions, Combust. Flame 156 (2009) 1799–1809.
[3] C.S. McEnally, L.D. Pfefferle, B. Atakan, K. Kohse-Hoinghaus, Studies of aromatic hydrocarbon formation mechanisms in flames: progress towards closing the fuel gap, Prog. Energy Combust. Sci. 32 (2006) 247–294.
[4] F. Carbone, A. Gomez, The structure of toluene-doped counterflow gaseous diffusion flames, Combust. Flame 159 (2012) 3040–3055.
[5] T. Edwards, L.Q. Maurice, Surrogate mixtures to represent complex aviation and rocket fuels, J. Propuls. Power 17 (2001) 461–466.
[6] W.J. Pitz, C.J. Mueller, Recent progress in the development of diesel surrogate fuels, Prog. Energy Combust. Sci. 37 (2011) 330–350.
[7] K. Gleason, A. Gomez, Detailed study of the formation of soot precursors and soot in highly controlled ethylene(/toluene) counterflow diffusion flames, J. Phys. Chem. A 127 (2023) 276–285.
[8] M. Frenklach, H. Wang, Detailed modeling of soot particle nucleation and growth, Proc. Combust. Inst. 23 (1991) 1559–1566.
[9] A. Matsugi, A. Miyoshi, Modeling of two- and three-ring aromatics formation in the pyrolysis of toluene, Proc. Combust. Inst. 34 (2013) 269–277.
[10] S. Sinha, A. Raj, Polycyclic aromatic hydrocarbon (PAH) formation from benzyl radicals: a reaction kinetics study, Phys. Chem. Chem. Phys. 18 (2016) 8120–8131.
[11] K.O. Johansson, J.Y.W. Lai, S.A. Skeen, D.M. Popolan-Vaida, K.R. Wilson, N. Hansen, A. Violi, H.A. Michelsen, Soot precursor formation and limitations of the stabilomer grid, Proc. Combust. Inst. 35 (2015) 1819–1826.
[12] K.O. Johansson, M.P. Head-Gordon, P.E. Schrader, K.R. Wilson, H.A. Michelsen, Resonance-stabilized hydrocarbon-radical chain reactions may explain soot inception and growth, Science 361 (2018) 997–1000.
[13] A. Hamins, D. Anderson, H. Miller, Mechanistic studies of toluene destruction in diffusion flames, Combust. Sci. Technol. 71 (1990) 175–195.
[14] A.M. Valencia-López, F. Bustamante, A. Loukou, B. Stelzner, D. Trimis, M. Frenklach, N.A. Slavinskaya, Effect of benzene doping on soot precursors formation in non-premixed flames of producer gas (PG), Combust. Flame 207 (2019) 265–280.
[15] K. Gleason, F. Carbone, A.J. Sumner, B.D. Drollette, D.L. Plata, A. Gomez, Small aromatic hydrocarbons control the onset of soot nucleation, Combust. Flame 223 (2021) 398–406.
[16] K. Gleason, F. Carbone, A. Gomez, Effect of temperature on soot inception in highly controlled counterflow ethylene diffusion flames, Combust. Flame 192 (2018) 283–294.
[17] H. Wang, Formation of nascent soot and other condensed-phase materials in flames, Proc. Combust. Inst. 33 (2011) 41–67.
[18] C.J. Dasch, Continuous-wave probe laser investigation of laser vaporization of small soot particles in a flame, Appl. Opt. 23 (1984) 2209.
[19] J.A. Sutton, J.F. Driscoll, Rayleigh scattering cross sections of combustion species at 266, 355, and 532nm for thermometry applications, Opt. Lett. 29 (2004) 2620–2622.
[20] G. Sutton, A. Levick, G. Edwards, D. Greenhalgh, A combustion temperature and species standard for the calibration of laser diagnostic techniques, Combust. Flame. 147 (2006) 39–48.
[21] A. D'Alessio, Laser light scattering and fluorescence diagnostics of rich flames produced by gaseous and liquid fuels, in: D.C. Siegla (Ed.), Part. Carbon, Springer, 1981, pp. 207–259.
[22] M.P. Bogaard, A.D. Buckingham, R.K. Pierens, A.H. White, Rayleigh scattering depolarization ratio and molecular polarizability anisotropy for gases, J. Chem. Soc. Faraday Trans. 1 Phys. Chem. Condens. Phases 74 (1978) 3008–3015.
[23] K. Gleason, F. Carbone, A. Gomez, PAHs controlling soot nucleation in 0.101—0.811MPa ethylene counterflow diffusion flames, Combust. Flame 227 (2021) 384–395.
[24] K. Gleason, F. Carbone, A. Gomez, Pressure and temperature dependence of soot in highly controlled counterflow ethylene diffusion flames, Proc. Combust. Inst. 37 (2019) 2057–2064.
[25] H.A. Michelsen, P.E. Schrader, F. Goulay, Wavelength and temperature dependences of the absorption and scattering cross sections of soot, Carbon N. Y. 48 (2010) 2175–2191.
[26] ANSYS CHEMKIN-pro release R2, (2019).
[27] Y. Wang, A. Raj, S.H. Chung, A PAH growth mechanism and synergistic effect on PAH formation in counterflow diffusion flames, Combust. Flame 160 (2013) 1667–1676.
[28] S. Park, Y. Wang, S.H. Chung, S.M. Sarathy, Compositional effects on PAH and soot formation in counterflow diffusion flames of gasoline surrogate fuels, Combust. Flame 178 (2017) 46–60.
[29] F. Carbone, F. Cattaneo, A. Gomez, Structure of incipiently sooting partially premixed ethylene counterflow flames, Combust. Flame 162 (2015) 4138–4148.
[30] L. Waldmann, K.H. Schmitt, Thermophoresis and diffusiophoresis of aerosols, Aerosol Sci. 137 (1966) 137–162.
[31] C. Russo, B. Apicella, A. Tregrossi, A. Ciajolo, K.C. Le, S. Török, P.E. Bengtsson, Optical band gap analysis of soot and organic carbon in premixed ethylene flames: comparison of in-situ and ex-situ absorption measurements, Carbon N. Y. 158 (2020) 89–96.
[32] A. D'Anna, Combustion-formed nanoparticles, Proc. Combust. Inst. 32 (2009) 593–613.
[33] M.R. Kholghy, G.A. Kelesidis, S.E. Pratsinis, Reactive polycyclic aromatic hydrocarbon dimerization drives soot nucleation, Phys. Chem. Chem. Phys. 20 (2018) 10925–10938.
[34] S.K. Friedlander, Dust Smoke, Haze, Fundamentals of aerosol behavior, John Wiley & Sons Inc, 1977.
[35] A. Raj, M. Sander, V. Janardhanan, M. Kraft, A study on the coagulation of polycyclic aromatic hydrocarbon clusters to determine their collision efficiency, Combust. Flame 157 (2010) 523–534.
[36] S.J. Harris, I.M. Kennedy, The coagulation of soot particles with van der Waals forces, Combust. Sci. Technol. 59 (1988) 443–454.
[37] C. Chu, T. Zhang, M.J. Thomson, The chemical structure effects of alkylbenzenes on soot formation in a laminar co-flow flame, Combust. Flame 204 (2019) 237–249.
[38] F.A. Williams, Combustion theory, 2nd ed., CRC Press, 1985, pp. 565–566. Appendix B.
[39] M. Frenklach, A.M. Mebel, Prenucleation chemistry of aromatics: a two-ring precursor? Proc. Combust. Inst. 38 (2022) 825–833.